Materials Today Bio 28 (2024) 101182

Contents lists available at ScienceDirect

Materials Today Bio

journal homepage: www.journals.elsevier.com/materials-today-bio

Long noncoding RNA MALAT1 mediates fibrous topography-driven pathologic calcification through trans-differentiation of myoblasts

Woo-Jin Kim [a,1], Jieun Bae [a,1], Eun-Hye Lee [a], Jaehyung Kim [a], Pil-Jong Kim [b], Peter X. Ma [c,d,e,f], Kyung Mi Woo [a,g,*]

[a] Department of Molecular Genetics, School of Dentistry and Dental Research Institute, Seoul National University, Seoul, 08826, Republic of Korea
[b] Biomedical Knowledge Engineering Laboratory, Dental Research Institute, Seoul National University, Seoul, 08826, Republic of Korea
[c] Department of Biologic and Material Sciences, School of Dentistry, University of Michigan, Ann Arbor, MI, 48109, USA
[d] Macromolecular Science and Engineering Center, University of Michigan, Ann Arbor, MI, 48109, USA
[e] Department of Biomedical Engineering, University of Michigan, Ann Arbor, MI, 48109, USA
[f] Department of Materials Science and Engineering, University of Michigan, Ann Arbor, MI, 48109, USA
[g] Department of Pharmacology & Dental Therapeutics, School of Dentistry, Seoul National University, Seoul, 08826, Republic of Korea

ARTICLE INFO

Keywords:
Prosthesis-induced pathologic calcification
Fibrous ECM mimicry
Trans-differentiation
Malat1

ABSTRACT

Prosthesis-induced pathological calcification is a significant challenge in biomaterial applications and is often associated with various reconstructive medical procedures. It is uncertain whether the fibrous extracellular matrix (ECM) adjacent to biomaterials directly triggers osteogenic trans-differentiation in nearby cells. To investigate this possibility, we engineered a heterogeneous polystyrene fibrous matrix (PSF) designed to mimic the ECM. Our findings revealed that the myoblasts grown on this PSF acquired osteogenic properties, resulting in mineralization both *in vitro* and *in vivo*. Transcriptomic analyses indicated a notable upregulation in the expression of the long noncoding RNA metastsis-associated lung adenocarcinoma transcript 1 (*Malat1*) in the C2C12 myoblasts cultured on PSF. Intriguingly, silencing *Malat1* curtailed the PSF-induced mineralization and downregulated the expression of bone morphogenetic proteins (*Bmps*) and osteogenic markers. Further, we found that PSF prompted the activation of Yap1 signaling and epigenetic modifications in the *Malat1* promoter, crucial for the expression of *Malat1*. These results indicate that the fibrous matrix adjacent to biomaterials can instigate *Malat1* upregulation, subsequently driving osteogenic trans-differentiation in myoblasts and ectopic calcification through its transcriptional regulation of osteogenic genes, including *Bmps*. Our findings point to a novel therapeutic avenue for mitigating prosthesis-induced pathological calcification, heralding new possibilities in the field of biomaterial-based therapies.

1. Introduction

Pathological calcification (PC) induced by prosthetic implants (PCI) is characterized by the abnormal accumulation of calcium and phosphate minerals within soft tissues and is often associated with various reconstructive medical procedures, including heart valve replacements, coronary artery grafting, and volumetric muscle regeneration. PCI can lead to vascular stiffness, hemodynamic disorders, and increased morbidity and mortality rates in cardiovascular diseases such as atherosclerosis, systolic hypertension, and coronary artery disease [1,2]. Various factors contributing to the processes of PCI have been identified, including material properties, host biological responses, and mechanical stresses on the implant. Based on these studies, strategies to mitigate pathological calcification have been developed, such as decellularization of valve tissues, chemical treatments to reduce immunogenicity, ion-loading fibrous matrices, and specific coatings that release anti-calcification agents [3–5]. Elucidation of the biological and material factors that contribute to calcification can provide insights into developing advanced materials and treatment methods that effectively prevent this process.

Abbreviations: ECM, extracellular matrix; PSF, polystyrene fibrous matrix; Malat1, metastasis-associated lung adenocarcinoma transcript 1; Bmps, bone morphogenetic proteins; Yap1, yes-associated protein 1.

* Corresponding author. 1 Gwanak-ro, Gwanak-gu, Seoul, 08826, Republic of Korea.
E-mail address: kmwoo@snu.ac.kr (K.M. Woo).

[1] These authors contributed equally.

https://doi.org/10.1016/j.mtbio.2024.101182
Received 4 March 2024; Received in revised form 14 July 2024; Accepted 3 August 2024
Available online 8 August 2024

In areas of calcification, collagen fibrils often exhibit significant disorganization, including fragmentation, misalignment, irregular fibril diameter, and altered cross-linking [6–9]. This disorganization of extracellular matrix (ECM) fibrils results in altered mechanical properties and provides sites for mineral nucleation. The onset of PCI is typically linked to alterations in the surface properties of implanted biomaterials [10]. While biological factors are known to be involved in pathological calcification, the onset of PCI is generally associated with changes in the surface properties of implanted biomaterials. After implantation, the biomaterial surface often becomes encased in a fibrotic matrix due to inflammatory reactions, and PCI originates from within this fibrotic matrix. It is worth noting that bacterial plaque formation can lead to the development of micro-/nano-fibrous structures on implant surfaces, particularly in aortic valves, where ectopic calcification frequently occurs along these fibrous structures [11]. While chronic inflammation resulting from external pathogenic infections can partially explain this phenomenon, calcification of the fibrotic matrix in sterile conditions remains unexplained.

Calcification in PCI is attributed to various mechanisms, including apoptosis and osteogenic conversion [10]. However, it is not yet clear whether the micro/nanostructure of the ECM in PCI-derived plaques directly induces calcification. ECM is a complex structure organized by biological factors and a fibrous three-dimensional (3D) structure. Both replicate a 3D structure with high roughness and hydrophilicity using a non-bioreactive polystyrene-based fibrous matrix (PSF). However, unlike PSF, ECM contains biological factors such as signaling molecules, cell-producing non-collagenous ECM components, extracellular vesicles, and microbial factors. Biomimetic biomaterials, such as hydrogel 3D scaffolds, micro/nano-grooved substrates, and electrospun fibrous membranes, feature hierarchical microstructures similar to the ECM, allowing them to modulate various cellular behaviors [4,10]. Electrospinning has been widely employed to fabricate fibrous biomaterials due to its ability to control topological cues, fiber density, chemical composition, and other physicochemical properties that influence cellular responses [12].

Previous research has shown that alterations in the 3D topography of nanofibers can induce the differentiation of mesenchymal stem cells into different cell lineages [13,14]. Nano-scale fibrous structures have been found to play a crucial role in chondrocyte differentiation and biomineralization [15]. In the context of biomaterial implants, ectopic calcification leads to the trans-differentiation of vascular smooth muscle (VSM) cells, primarily through bone morphogenetic protein (BMP) and Wnt signals resulting from mechano-transduction between the vascular matrix and VSM cells [16]. However, the exact mechanism by which mechano-transduction influences the expression of osteogenic signals, BMP, and Wnt, in vascular smooth muscle cells remains unclear.

Metastasis-associated lung adenocarcinoma transcript 1 (Malat1) is an exceptionally long long non-coding RNA (lncRNA), whose critical roles have emerged in various biological processes, including cell division, survival, motility, transcription, translation, and RNA splicing [17]. It has been extensively studied for its regulatory functions in cancer metastasis and its role as an epigenetic modulator in metabolic diseases, neuropathic diseases, and cancer metastasis [18–20]. Mechanistically, Malat1 regulates nuclear speckle organization associated with m6A modifications and participates in the formation of histone methyltransferase complexes [21]. Conversely, the methylation status of the Malat1 promoter plays a crucial role in regulating its expression, with Mettl3, an m6A methyltransferase, known to inhibit Malat1 expression [21,22].

In this study, we demonstrated that a heterogeneous ECM mimicry created using electrospun polystyrene micro/nanofiber sheets (PSF) could directly induce ectopic calcification of myoblasts without the need for chemical or biological cues. Despite polystyrene's typical biocompatibility and bio inert properties [23,24], the 3D topological differences of PSF led to ectopic calcification in muscle tissue. Furthermore, myoblasts cultured on the ECM-mimicking PSF exhibited reduced myogenic differentiation and enhanced osteogenic differentiation. Mechanistically, this was attributed to Yes-associated protein 1 (*Yap1)* signaling inducing the expression of *Malat1*, a lncRNA implicated in PSF-induced ectopic calcification. These findings suggest the direct role of the ECM micro/nanostructure in pathologic calcification induced by implanted prostheses.

2. Methods

2.1. Preparation of the PSF matrix

The PSF matrix was electrospun as previously described [25], using polystyrenes (Mw 350,000 g/mol, Mw 280,000 g/mol, Sigma) dissolved in N, N-dimethylformamide: Dichloromethane = 3: 2 (Sigma) (10 % w/v). The solution was rotated overnight at room temperature, injected through a 32G syringe needle, and injected at a flow rate of 0.1 ml/h. The syringe needle was connected to a high voltage DC power supply (Chungpa EMT, Korea) of 15 kV. The resulting PSF sheet was air-dried, immersed in DPBS, washed with 70 % ethanol, and UV-dried before cell culture.

2.2. Surface topography analysis

The surface topography of the PSF matrix was analyzed as previously described [25]. Surface roughness and topographical measurements were determined under a confocal microscope (Carl Zeiss LSM 800, Oberkochen, Germany). The surfaces of PSF and high-density polytetrafluoroethylene (PTFE) were analyzed using ConfoMap software. The contact angle was measured by the sessile drop method using an image analyzer equipped with a video camera (Phoenix 300, Surface Electro Optics, Seoul, Korea). Bacterial culture dishes (BCD) was coated with BD Cell-Tak™ to assess cellular behavior in relation to surface structural differences. The coated BCD is referred to as BCD_{coated}. PSF and BCD were treated with 70 % $HClO_4$ to enhance hydrophilicity for improved cell adhesion properties, similar to conventional culture substrate condition (TCD).

2.2.1. Scanning electron microscopy (SEM)

Cultured cells were rinsed in PBS, fixed using 2.5 % glutaraldehyde in a 0.1 M cacodylate buffer (pH 7.4) and freeze-dried. The specimen was dehydrated by dipping it in increasing concentrations of ethanol and then by critical point drying. After drying, the fragment was sputter-coated with gold-palladium and observed under an SEM (FE-SEM Hitachi S-4700, Japan) at 12 kV, 100× magnification. PSFs without cells were sputter-coated with platinum and observed under an SEM (FE-SEM Hitachi S-4700, Japan) at 12 kV, 10000× magnification.

2.3. In vivo transplantation

Ectopic calcification induced by PSF was evaluated in C57BL/6 mice, with Cytoplast™ TXT-200 (Osteogenics Biomedical, Lubbock, TX, USA) as control. Mice were anesthetized with Zoletil (0.4 ml/kg) and Rompun (10 mg/kg). Control and experimental groups were randomly allocated to avoid possible biases. The material was implanted into the internal space of vastus medialis and gracilis in each leg muscle and sutured. Experimental procedures followed protocols approved by the Institutional Animal Care and Use Committee of Seoul National University (SNU-230508-1-2).

2.4. Hematoxylin & eosin (H&E) staining and Immunohistochemistry (IHC)

After 12 weeks, the mice were sacrificed for evaluation. H&E staining was performed by Oben Bio (Seoul, Korea). For IHC, sections were deparaffinized and antigen retrieval was done using the heat-induced epitope retrieval method. Slides were washed with TBS containing

0.025 % Triton X-100 (TBS-T) for 5 min, twice, and then blocked with 1 % BSA in TBS for 2 hrs at room temperature. The slides were drained for a few seconds, and excess blocking buffer was wiped off with tissue paper. Slides were incubated with anti-Runx2 antibody (Santa Cruz Biotechnology) overnight at 4 °C. Alexa Fluor 488 and 647 conjugated goat anti-rabbit secondary antibodies (Invitrogen, Grand Island) were used. To identify the nuclei, mounting medium with 4′,6-diamidino-2-phenylindole (DAPI; Vector Labs, Burlingame) was used. The samples were observed with a confocal microscope (LSM 800, Carl Zeiss).

2.5. Von kossa staining

The paraffin-embedded *in vivo* samples were deparaffinized and rinsed with distilled water. Calcium deposition was detected by treating the sections with 5 % silver nitrate solution and exposing them to UV light for 1 h. The slides were then rinsed multiple times with deionized water, and unreacted silver was removed using 2 % sodium thiosulfate for 5 min. Finally, the slides were washed with deionized water again, dehydrated, and mounted with Permount.

2.6. Cell culture

C2C12 mouse myoblasts were maintained in growth medium [GM; DMEM (Hyclone, Logan) with 10 % (v/v) fetal bovine serum (FBS, Hyclone) and 100 U/mL of penicillin-streptomycin (Hyclone)] at 37 °C in a humidified incubator with 5 % CO_2. Osteoblast differentiation was induced using osteogenic medium [OM; the GM with 50 μg/ml ascorbic acid (Sigma) and 10 mM β-glycerophosphate (Sigma)], with medium changes every two days.

2.7. Alkaline phosphatase (ALP) staining

C2C12 were cultured in GM and OM in a 24-well plate. After seven days of induction, the cells were fixed using 4 % paraformaldehyde. ALP staining was assessed with *p*-nitrophenyl phosphate (*p*-NPP, Thermo Fisher Scientific) as a substrate. Cells added with the substrate were placed in 37 °C for 10 to20 min for the reaction to occur. The reaction was stopped by washing with DPBS three times.

2.8. Alizarin Red S (ARS) staining

C2C12 cells were cultured in osteogenic medium in a 24-well plate. After 21 days post-induction, the cells were fixed with 4 % paraformaldehyde for 30 min at room temperature. Subsequently, the cells were rinsed with phosphate-buffered saline (PBS) and stained with Alizarin Red S dye (Sigma) at pH 4.15. The images of the staining were analyzed using ImageJ software.

2.9. In vitro cell viability assay

C2C12 cells were seeded into a 96-well plate and cultured for four days. The osteogenic medium was changed every two days, and the CCK8 reagent was added and incubated for 30 min to 1 h to measure absorbance at 450 nm. To identify apoptotic cells, a TUNEL assay was performed using the DeadEnd™ Fluorometric TUNEL System (Promega) following the manufacturer's instructions.

2.10. Total RNA sequencing

Total RNA from cells cultured on TCD and PSF was extracted using QIAzol Lysis Reagent (QIAGEN, Valencia, CA). RNA concentration was measured by Quant-iT RiboGreen (Invitrogen) and quality and integrity were assessed using the TapeStation RNA screentape (Agilent). RIN greater than 7.0 was selected for RNA library construction. Illumina TruSeq Stranded Total RNA Library Prep Gold Kit (Illumina, Inc., San Diego, CA, USA) was used for library preparation. From the total RNA sample, rRNA was depleted to detect mRNA and lncRNA. Then, samples were fragmented into small pieces and first-strand cDNAs were copied using SuperScript II reverse transcriptase (Invitrogen) and random primers. Second-strand cDNA was synthesized by adding DNA polymerase I, RNase H and dUTP. Subsequently, the products were purified and enriched with PCR to create the final cDNA library.

The libraries were quantified with KAPA Library Quantification kits for Illumina Sequencing platform according to the qPCR Quantification Protocol Guide (Kapa Biosystems) and qualified using the TapeStation D100 ScreenTape (Agilent Technologies). Indexed libraries were then submitted to Illumina NovaSeq6000 (Illumina), and the paired-end (2 x 100 bp) sequencing was performed by Macrogen (Seoul, Korea).

2.11. Real-time quantitative polymerase chain reaction (RT-qPCR)

Total RNAs of cells cultured on TCD and PSF were extracted using QIAzol Lysis Reagent (Qiagen). Then, cDNA was synthesized using PrimeScript RT Reagent Kit with gDNA Eraser (Takara) according to the protocol provided. RT-qPCR was performed on real-time PCR system (Applied Biosystems) using TB Green Premix Eq *Taq*II, ROX plus (Takara). The relative expression levels were calculated with the comparative threshold cycle method and each target gene transcript was normalized using glyceraldehyde-3-phosphate dehydrogenase (Gapdh) level. The PCR primers sets are listed in the Supplementary Table.

2.12. Whole-genome bisulfite sequencing (WGBS)

Library preparation for bisulfite sequencing was done using SureSelectXT Methyl-Seq Target Enrichment System for Illumina Multiplexed Sequencing (Agilent). DNA quality, quantity and concentration were measured by Qubit (Thermo Fisher Scientific) and Nanodrop. Each genomic DNA sample was fragmented into 100–200 bp using Covaris. Following fragmentation, end-repair and adaptor ligation were done. Captured targets were pulled down by biotinylated probe using streptavidin-coated magnetic beads (Dynabeads MyOne Streptavidin T1; Life Technologies Ltd.). Bisulfite conversion was performed with EZ DNA Methylation-Gold kit (ZymoResearch) and the bisulfite-treated libraries were amplified with indexed primers. Paired-end (2 x 151 bp) sequencing was done using Illumina NovaSeq6000 (Illumina) by Theragen Bio Incorporation.

2.13. Alignment, methylation calling and analysis

The bisulfite-treated sequencing readers were aligned to the mouse reference genome (mm10) using Bismark v0.24.2 [26]. The alignment was conducted using default parameters, which are optimized for high-throughput sequencing data. Following alignment, methylation states at individual cytosine positions in CpG context were extracted using the bismark_methylation_extractor module of the Bismark software. This module enables the identification and annotation of methylated and unmethylated cytosines along with their genomic positions.

For analysis of differentially methylated regions (DMRs), DMRichR v1.7.8 was employed [27]. The analysis commenced with loading the methylation data alongside the mm10 genomic annotation. This was managed using the GenomicRanges package v1.54.1 to handle range-based data and the TxDb.Mmusculus.UCSC.mm10.ensGene database for gene annotations. The default parameters for DMRichR functions were applied. The plotDMRs function in DMRichR was utilized to visualize the identified DMRs.

2.14. Knockdown assay with siRNA transfection

C2C12 cells seeded at 1.0×10^4 cells/well at 6-well plate for seven days with OM and *Malat1* siRNA (Dharmacon) were transfected for 48 hrs. The concentration of both the siRNA and negative control was 10 nmole using DharmaFECT Transfection Reagent following the

manufacturer's instructions.

2.15. Immunofluorescence assay

The cultured cells were fixed with 4 % paraformaldehyde, permeabilized with PBS containing 0.1 % Triton X-100 (PBS-T), and blocked in PBS-T with 5 % bovine serum albumin (BSA). The cells were incubated with anti-Bmp2, Bmp7 and Yap1 antibodies (Abcam, Santa Cruz Biotechnology), followed by Alex Fluor 488 and 647 conjugated-goat anti-rabbit secondary antibodies (Invitrogen). Rhodamine phalloidin (Invitrogen) was added to appeal the actin. A mounting medium with DAPI (Vector labs, Burlingame) was used to identify the nuclei. The samples were observed with confocal microscope (LSM 800, Carl Zeiss). The image analyses were done with the Zen (Carl Zeiss) software.

2.16. Western blot analysis and cell fractionation

Cells were lysed with RIPA lysis buffer [50 mM Tris-HCl (pH 7.5, Biosesang, Suwon, Korea), 0.15 M Sodium chloride, 1 % Triton X-100, 1 % Sodium deoxycholate, 0.1 % Sodium dodecyl sulfate (SDS), 2 mM EDTA and complete protease inhibitor cocktail solution (Sigma)]. For nuclear and cytoplasm fractionation, NE-PER Nuclear and Cytoplasmic Extraction Reagent (ThermoScientific) was used following the manufacturer's instruction. Proteins were separated on 10 % SDS-polyacrylamide gel electrophoresis (PAGE) and transferred onto a poly (vinylidene difluoride) membrane. After blocking with 5 % nonfat skim milk in TBS-T buffer (10 mM Tris-HCl, pH 7.5, 100 mM NaCl and 0.05 % Tween-20), the membrane incubated with specific primary antibodies and then HRP-conjugated secondary antibodies. ECL reagent (Bio-Rad) was applied, and the signals were detected with Bio-Image Analyzer (Bio-Rad,). β-actin and Lamin B1 served as loading controls.

2.17. Chromatin immunoprecipitation (ChIP) assay

C2C12 cells were cultured on polystyrene nanofibers in osteogenic media at a density of 3.5×10^4 cell/dish. After seven days, the cells were fixed with 37 % formalin and 5 ml PBS (final concentration of 1 %) for 10 min. The reaction was quenched with 2.0 M glycine (final concentration of 125 mM) for 10 min. PBS/formalin/glycine were removed, and the cells were washed gently with ice-cold PBS, and trypsin was added to detach the cells. Cells were suspended with cold PBS, PMSF (final concentration of 200 mM) and proteinase inhibitor and centrifuged at 360×*g* for 5 min at 4 °C. The supernatant was removed, and RIPA lysis buffer were added. Samples were sonicated on ice to fragment at a size of 200 bp – 500 bp. Sheared chromatin was cleared by centrifugation at 13000×*g* for 10 min at 4 °C.

Immunoprecipitation with Tcf3 and Tead1 antibody (Santa Cruz Biotechnology) was performed using Dynabeads Protein G (Invitrogen) following the manufacturer's instruction. Crosslinks were reversed using elusion buffer (1 % SDS, 0.1 M $NaHCO_3$) and the sample was transferred into a new tube and incubated at 95 °C for 15 min with 5 M NaCl. DNA was recovered using Phenol:Chloroform:Isoamyl Alcohol (Avantor) following the manufacturer's instructions. Immunoprecipitated fragments were analyzed by RT-qPCR with IgG as a control.

2.18. Calcium detection

C2C12 cells were seeded in 6-well tissue culture plate at a density of 1×10^6 cells per well and cultured overnight in DMEM with 10 % fetal bovine serum. Cell culture medium was changed into osteogenic medium and differentiated for 24 hrs. For Ca^{2+} detection, Ca^{2+} was labelled using Rhod-2, AM, cell permeant at 1 μM concentration for 1 h at 37 °C. The fluorescence intensity was observed by confocal microscope (LSM 800, Carl Zeiss).

2.19. Statistical analysis

All the experiments in this study were repeated at least three times. Representative data are presented with averages and standard deviations. Statistically significant differences were analyzed using ANOVA ($p < 0.05$). Quantification analysis of SEM and immunofluorescence staining was done using the Fiji software. PSF and PTFE direction of orientation was measured using OrientationJ Distribution plugin in the Fiji software.

3. Results

3.1. The transplantation of a heterogeneous polystyrene nanofiber induced ectopic calcification in vivo

Electrospinning has been a well-established technique for fabricating fibrous scaffolds that mimic the ECM for several decades [28,29]. To closely emulate the natural ECM, we employed the electrospinning process to create PSF with nano-to micro-sized and heterogeneous orientations. In contrast to the random orientations and varying size distributions exhibited by the PSF, the non-resorbable PTFE, possesses a relatively smooth surface (Fig. 1a). Compared to TCD, the surface coated with PSF exhibited a higher average height roughness (Ra) and an increased surface roughness (Sa). This diverse nano/micro fibrillation of polystyrene significantly augmented the surface properties of PSF which resembles the 3D topology of ECM. The PSF demonstrated a heterogeneous size distribution and exhibited a higher degree of irregularity compared to PTFE, as evidenced by the measurements of surface orientation angles (Fig. 1b and c). When compared to commercialized PTFE, PSF showed similar hydrophobicity but demonstrated a more compact and fibrous structure (Fig. 1d).

To investigate whether these ECM-like PSF induced pathological calcification following transplantation, we implanted the PSF into the intermuscular space between the gracilis and adductor muscles in the posterior thigh of mice. A PTFE membrane was used as a control because it exhibited homogeneously thick, aligned fibers. From the 4^{th} to the 8^{th} week post-transplantation, we noted lamellar calcification patterns predominantly in the intermuscular space where the PSF was implanted, mirroring the implant's footprint. Conversely, the control group showed only inflammatory tissue around the implants, as seen in Fig. 2a. The Von Kossa staining results of the PSF implant sites showed mineralization patterns consistent with the H&E staining results (Fig. 2b). Similarly, the anti-Runx2 IHC results confirmed the presence of mineral deposits, indicating successful osteogenic differentiation on the PSF scaffolds (Fig. 2c). Additionally, soft X-ray and μCT analyses further verified the emergence of new ectopic calcifications within the muscle tissue after PSF implantation, detailed in Fig. 2d.

3.2. Myoblasts cultured on PSF without stimulation underwent osteogenic differentiation by secreting endogenous BMPs

C2C12 myoblast precursor cells typically undergo spontaneous myogenic differentiation [30]. However, when these cells were cultured on PSF, they showed mineralization without requiring additional exogenous signals for osteogenic differentiation, as illustrated in Fig. 3a. Additionally, consistent with the ALP staining results, *in vitro* mineral deposition was also confirmed in the ARS staining results **(Supplementary Fig. 1a).** This mineralization in the culture of C2C12 cells on PSF was observed even in standard GM that lacked specific osteogenic

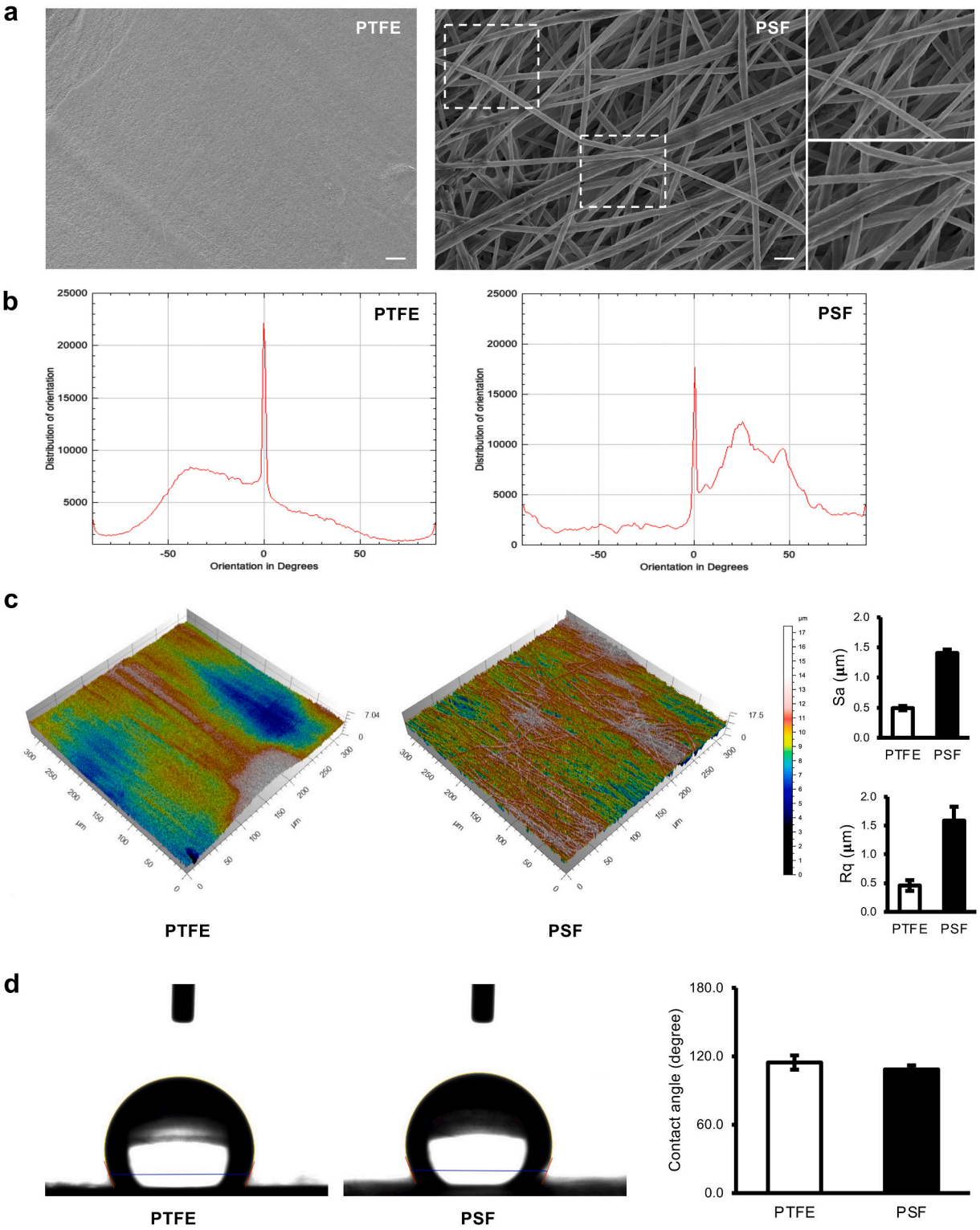

Fig. 1. Characterization of PSF in comparison with a control PTFE.
(a) Scanning electron microscopy. Magnification; 3000× (PSF inlet, 20000x), Scale bar = 10 μm (b) Degree of orientation analysis. PSF shows a random orientation distribution while PTFE does an even one. (c) Surface roughness. Quantitative analysis showed a notably increased surface roughness and arithmetic average of 3D roughness in PSF. (d) Water contact angle. PSF does not show significant differences in surface hydrophobicity. All data present with averages and standard deviations (n = 3).

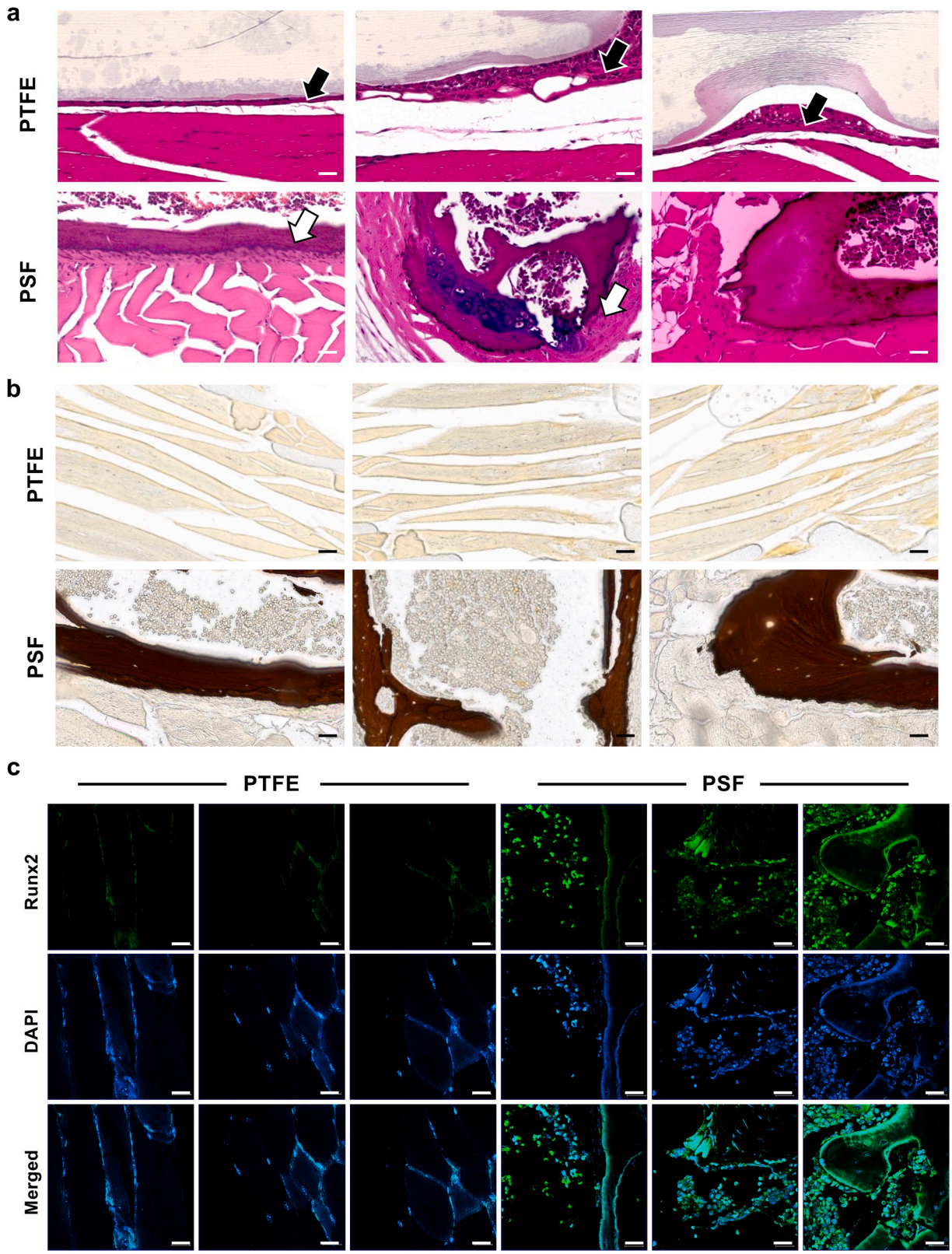

Fig. 2. PSF induces ectopic calcification *in vivo*.
(a) Hematoxylin and eosin staining. PSF was implanted into the interal space of vastus medialis and gracilis muscles. After 12 weeks post-transplantation, the mice were sacrified and evaluated for ectopic calcification. Scale bar = 5 μm. (b) Von kossa staining. Scale bar = 5 μm. (c) Immunohistochemistry for Runx2. Green; Runx2. Blue; Nuclei. Scale bar = 20 μm. (d) Soft X-ray and μCT analysis. Scale bar = 5 μm.

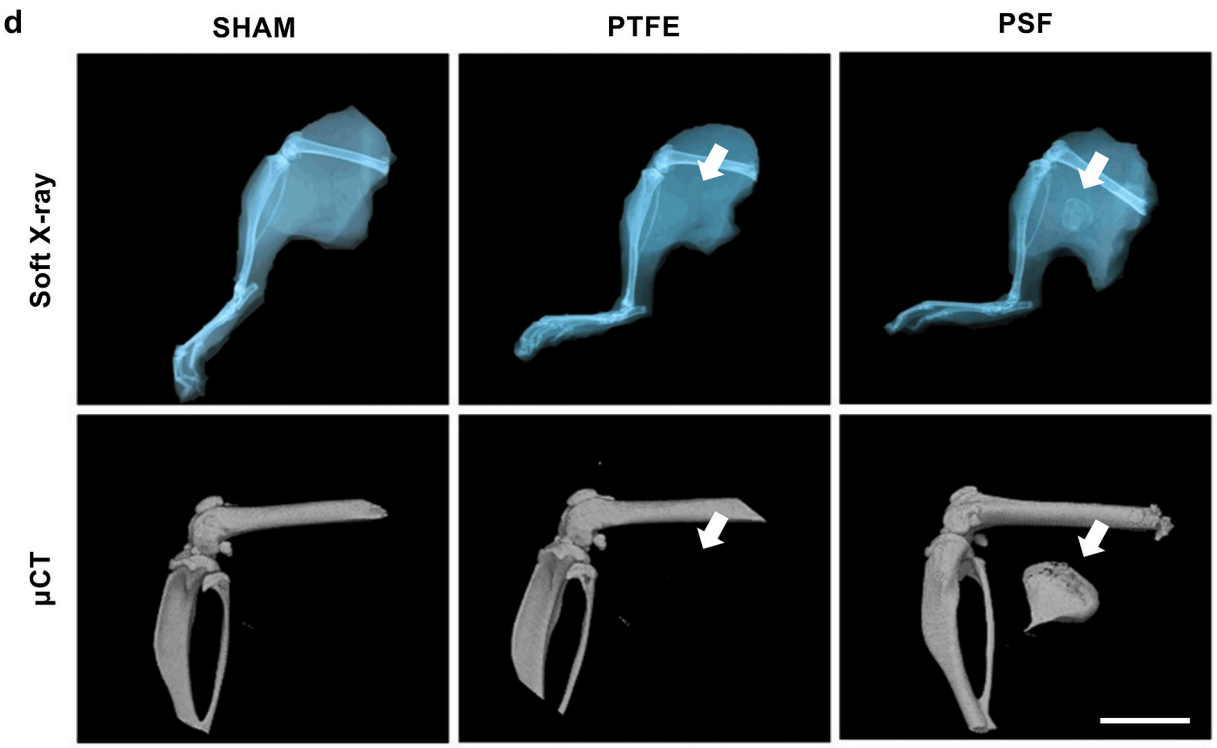

Fig. 2. (*continued*).

supplements. Additionally, the mineralization intensity increased when the cells were cultured in OM. In contrast, C2C12 cells grown on a TCD did not exhibit mineralization in either GM or OM. The osteogenic differentiation of C2C12 cells on the micro/nanofibrous architecture of PSF could be further enhanced by treatment with exogenous Bmp2 (Fig. 3a) and was inhibited by the physiological Bmp antagonist, Noggin (Supplementary Fig. 2).

C2C12 myoblasts cultured on the ECM-mimicking PSF, featuring micro/nanofibrous architecture, diverted from their typical muscle differentiation path, favoring osteoblast differentiation instead. Contrary to the cells in TCD, C2C12 cells on PSF retained a mononuclear structure, avoiding differentiation into multinucleated muscle cells. Furthermore, the expression of osteogenic markers, *Osteocalcin* (*Ocn*) and *Osterix* (*Osx*), increased consistently, and myogenic marker genes (*Myogenin* and *MyoD*) were decreased in the PSF group (Supplementary Fig. 3). Furthermore, the C2C12 cells cultured on PSF did not show any significant cytotoxicity (**Supplementary Figs. 1b–c**).

Bmp2 and Bmp7 are crucial growth factors for osteogenic differentiation in C2C12 cells and inducing ectopic calcification *in vivo* [31,32]. Conversely, Bmp4 treatment results in myogenesis or chondrogenesis in C2C12 cells, rather than osteogenesis [33]. The PSF induced distinct morphological and growth changes in C2C12 cells. While cells on TCD exhibited the typical elongated morphology, those on PSF displayed a reduced cytoplasmic area and more significant growth in the Z-axis direction, as depicted in Fig. 3b. The cell spreading area on PSF was about 45 % smaller compared to TCD (Fig. 3c).

We hypothesized that the mineralization observed in the C2C12 myoblasts culture on PSF's micro/nanofibrous architecture was driven by Bmp signals. The expression of *Bmp2* and *Bmp7* genes was higher in PSF than in TCD and was further enhanced by OM treatment. In contrast, the expression of *Bmp4* showed no significant difference. Particularly, the activation of R-SMAD following BMP signaling was strongly observed in PSF (Fig. 2d and Supplementary Figure 4). Immunofluorescence confirmed that cells on PSF secreted higher levels of Bmp2 and Bmp7 than those on TCD. Furthermore, the secretion of Bmp2/7 increased with Bmp2 exhibiting a more pronounced intercellular distribution than Bmp7, as shown in Fig. 3e and f. Furthermore, the induction of these Bmp signals was driven solely by changes in 3D topology and was independent of the material properties. In two groups with similar surface structures but different hydrophobicity, such as BCD and TCD, the expression of *Bmp2* and SMAD signaling genes were consistently low, while those were notably high in PSF (Supplementary Figure 5).

3.3. The upregulation of Malat1 on the PSF augmented osteogenic differentiation

Comprehensive RNA sequencing (RNA-seq) analysis of cells cultured on PSF and TCD revealed the regulatory targets underlying the trans-differentiation induced by PSF. After sevendays in OM, both PSF and TCD exhibited distinct difference in their transcriptome, as evident from PCA analysis (Fig. 4a). In the PSF group, of most significantly upregulated genes was *Malat1*, a lncRNA, ranking first among the top 20 genes with increased expression (Fig. 4b). We conducted differential expression gene (DEG) analysis on a set of 5803 genes with fold change (FC) $\geq$ 1.5 and p-value $\leq$ 0.05. Compared to the TCD group, the PSF group exhibited an increase in the expression of 168 genes and a decrease in 1451 genes (Fig. 4c).

The up-regulated genes among the DEGs were notably associated with various terms related to osteogenic differentiation. Conversely, the down-regulated genes among the DEGs were linked to myogenic differentiation and cell proliferation (Fig. 4d). In the Gene Set Enrichment Analysis (GSEA) analysis, processes related to ossification and biomineralization were consistently observed to be significantly enriched

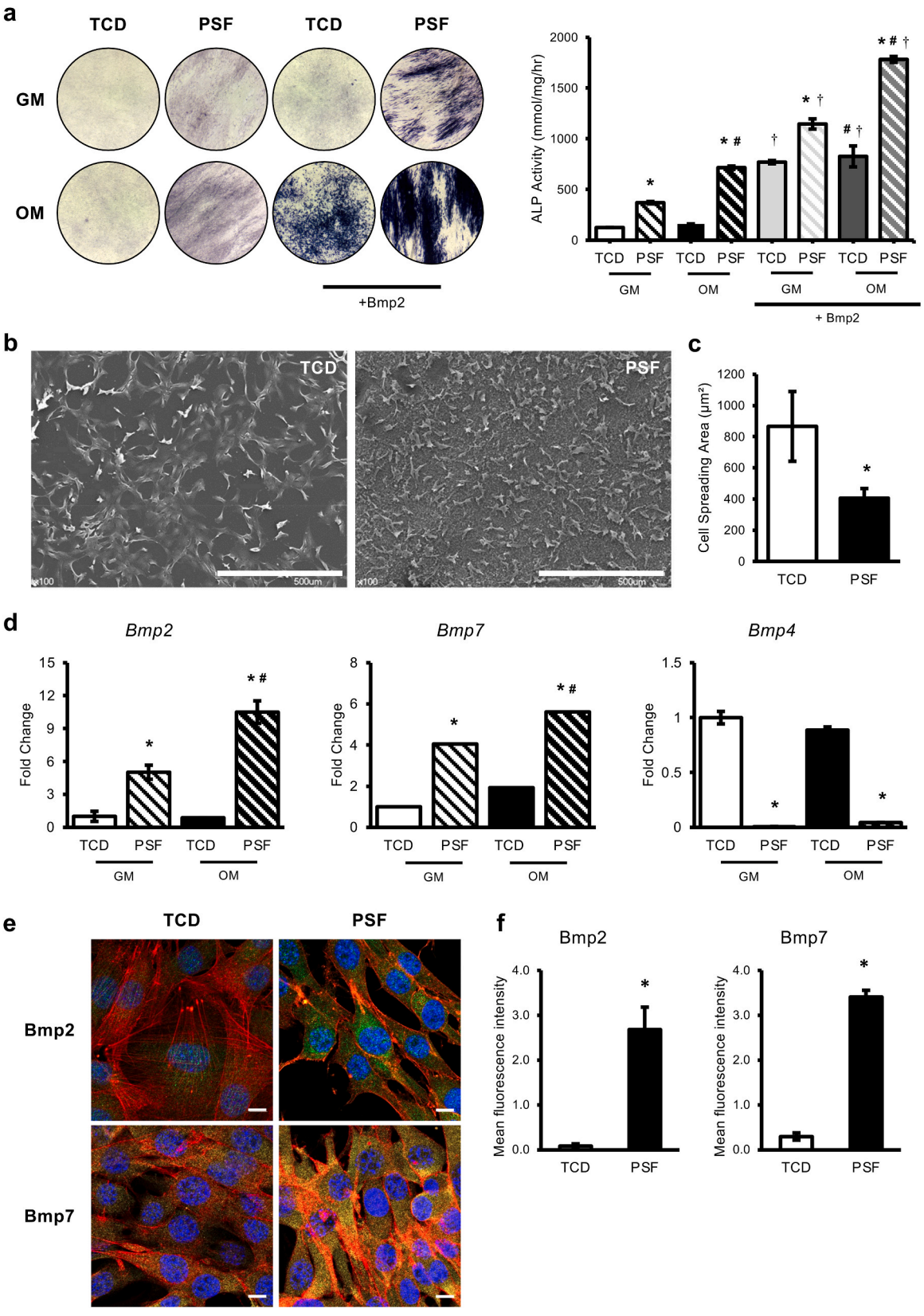

Fig. 3. PSF induces osteogenic phenotype and activates Bmp signaling in myoblast cells.
(a) Alkaline phosphatase staining and activity. The C2C12 myoblasts were cultured on PSF for 1 week. (b) SEM images of C2C12 cells grown on TCD and PSF. Scale bar = 500 μm. (c) Quantification of cell spreading. The cell area was measured from the SEM images. (d) Expression of *Bmp2*, *Bmp7* and *Bmp4* transcripts. The RT-qPCRs were performed, and *Gapdh* was used for normalization. (e) Immunostaining for Bmp2 and Bmp7 proteins in the cells grown on TCD and PSF. (Green: Bmp2, Yellow: Bmp7, Red: actin phalloidin, Blue: DAPI). The C2C12 myoblasts were cultured on TCD and PSF for four days. Statistical data present with averages and standard deviations (n = 3). Scale bar = 20 μm. (f) Mean fluorescence intensity of Bmp2 and Bmp7. * Statistically different (TCD vs. PSF; $p < 0.05$). # Statistically different (GM vs. OM; $p < 0.05$). † Statistically different (Non-treated vs. BMP2- treated; $p < 0.05$).

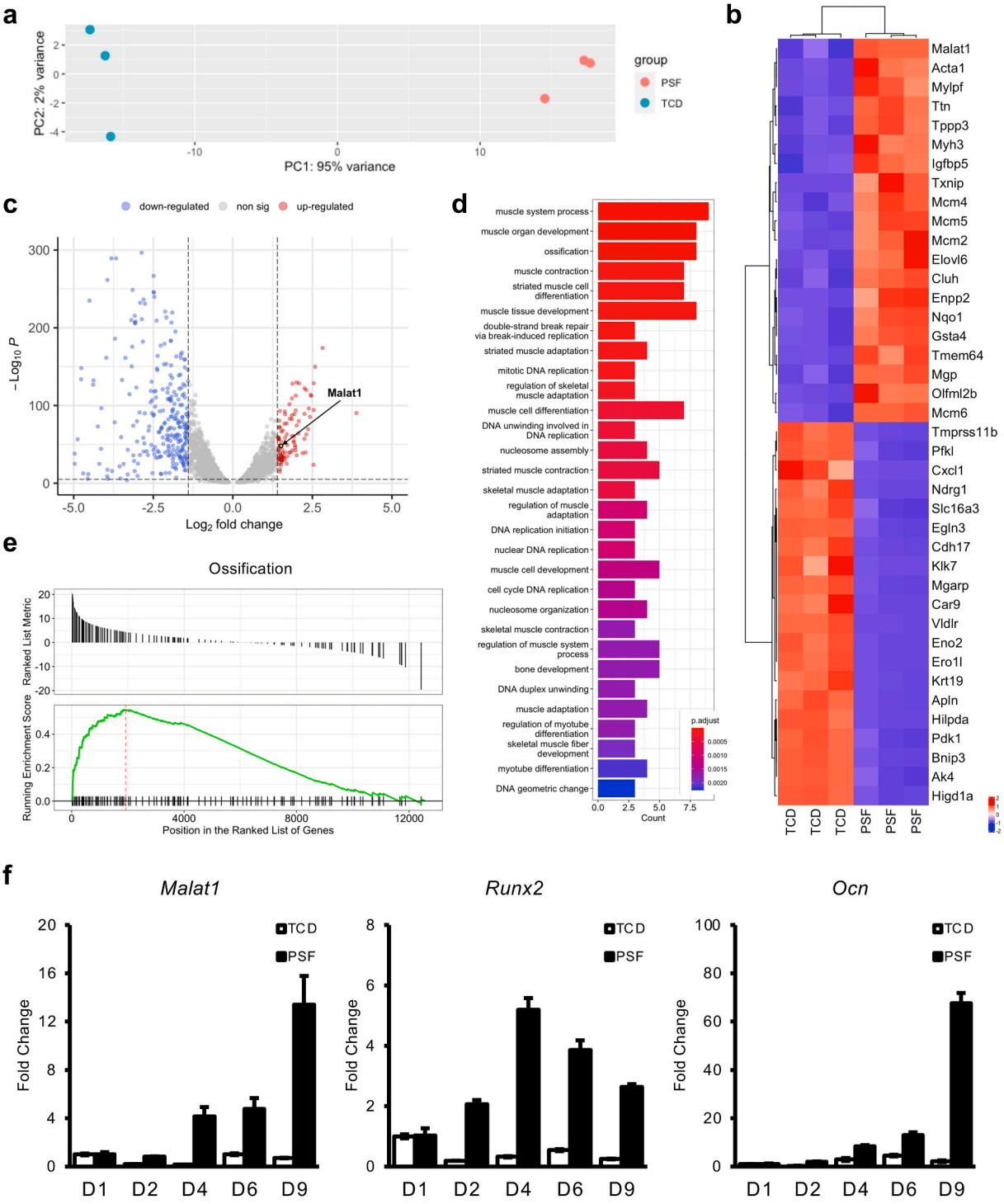

Fig. 4. Total RNA sequencing reveals an increase of *Malat1* expression in PSF group.
(a) PCA analysis of Total RNA-seq result of PSF and TCD groups. (b) Heatmap of significant differential genes of PSF and TCD groups. (c) Volcano plot described differential expressed genes in PSF/TCD. (d) Biological process analysis of DEGs. (e) GSEA analysis of significant biological process; Ossification (f) RT-qPCR validation of expression level of *Malat1* and osteogenic marker genes. Data present with averages and standard deviations (n = 3).

(Fig. 4e). The RT-qPCR validation of key genes, including *Malat1*, exhibited a consistent pattern with the RNA-seq findings (Fig. 4f).

3.4. The PSF induced demethylation of the Malat1 promoter in myoblasts

The transcriptomic changes observed in the cells on PSF in the absence of specific growth factor stimulation appear to be attributable to variations in DNA methylation. We performed bisulfite sequencing of C2C12 cells cultured on both PSF and TCD to identify DNA methylation patterns in each condition. The results revealed no significant differences in total DNA methylation level between the two conditions (Fig. 5a). However, CpG-associated regions displaying differential methylation levels in PSF compared to TCD were primarily the promoter region and distal intergenic region, accounting for a total of 60% of the

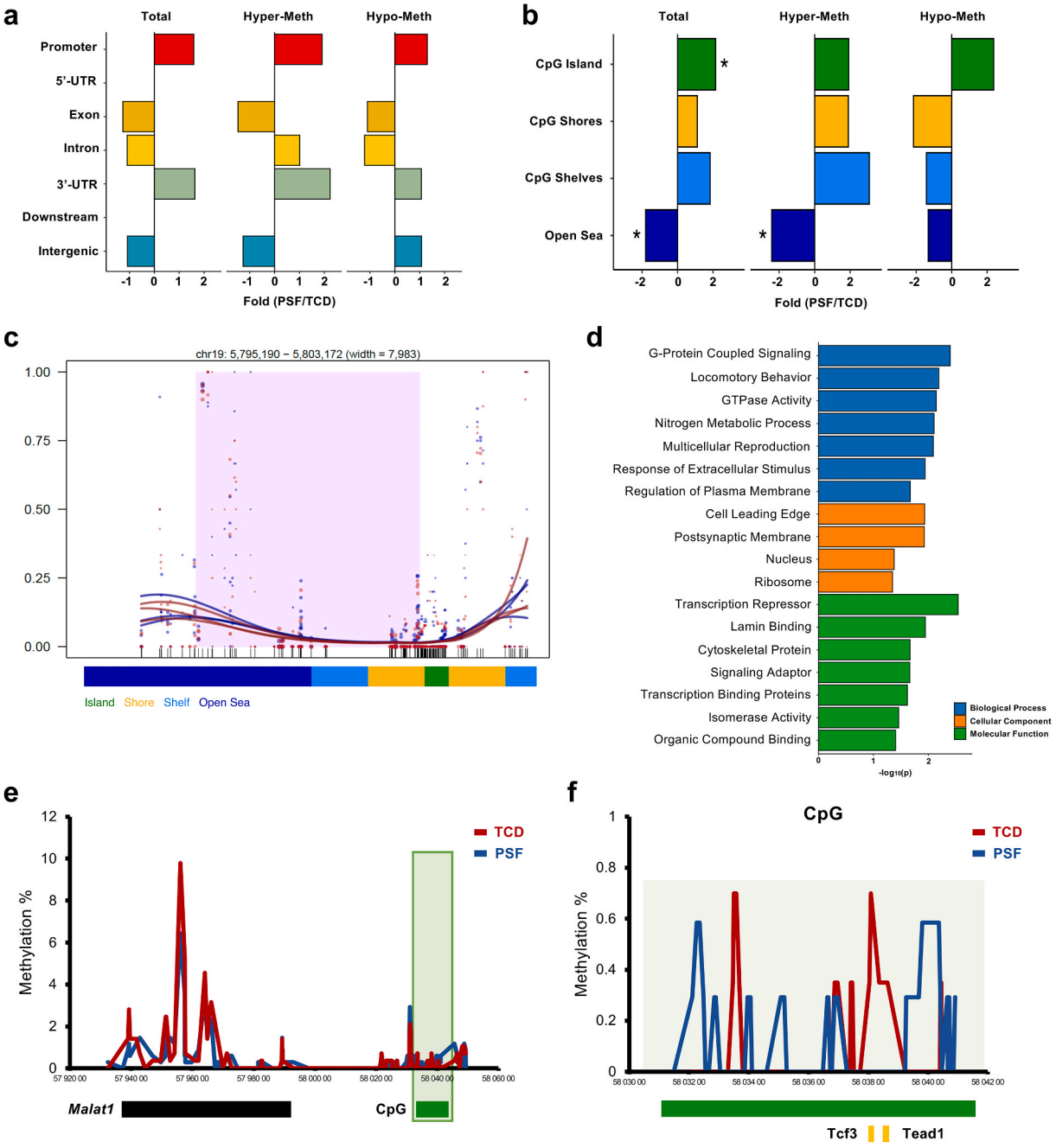

Fig. 5. Bisulfite sequencing results shows a decrease in the CpG methylation level of *Malat1* in the PSF group.
(a) Visualization of whole-genome bisulfite sequencing (WGBS) data using Integrated Genome Visualizer (IGV). Differentially methylated regions (DMRs) is observed between TCD and PSF. (b) Differentially methylated regions in CpG regions. (c) Significant differential regions in chromosome 19. (d) Enrichment analysis of DMR related genes. (e) The upstream region of *Malat1* in PSF shows more demethylated region compared to TCD. (f) The CpG region of *Malat1* in PSF shows more demethylated region compared to TCD. Red = TCD/Blue = PSF.

differential methylation patterns (Fig. 5b). Over-representation analysis performed on representing region exhibiting differential methylation levels within ±2 kb of the promoter and CpG regions revealed that the PSF group increased in methylation for genes associated with myogenic differentiation and cell proliferation terms but decreased in methylation for genes linked to osteogenic differentiation (Fig. 5c).

Methylation sequencing (Methyl-seq) unveiled a significant correlation between genes associated with DMR and their expression levels as revealed by RNA-seq. In particular, the GSEA results for the top 100 genes that were hyper-methylated and had reduced RNA expression levels indicated a significant decline in biological processes related RNA-seq (Fig. 5d).

The differential expression of *Malat1* in the C2C12 cells cultured on PSF stemmed from alterations in the methylation levels of its promoter region. Notably, a pronounced demethylation was observed in the CpG region and distal regions of the *Malat1* gene in cells cultured on PSF. Specifically, methylation in the upstream 4 kb region of the promoter, the 3′UTR region dramatically decreased in the PSF group (Fig. 5e). The methylation levels increased in the 2 kb region adjacent to the *Malat1* CpG island in TCD. Motif analysis of the *Malat1* promoter region indicated the presence of binding sites for Tead1 and Tcf3. Notably, the methylation levels showed significant variation near these Tead1 and Tcf3 binding sites (Fig. 5f).

3.5. *Yap1 translocation, activated by the PSF, led to the induction of Malat1 expression*

As consistently observed in RNA-seq and Methyl-seq analyses, 3D topology of PSF facilitated the response to extracellular stimuli, and predicted Yap signaling as a key factor. In the C2C12 cells cultured on PSF, we observed no significant differences in total Yap1 protein expression levels compared to those on TCD. However, the PSF group exhibited a marked increase in nuclear localization of Yap1 protein, as shown in Fig. 6a and b. The increased nuclear translocation of Yap1 in PSF was reduced by the knockdown of *Malat1* (Fig. 6c).

The increase in nuclear Yap1 protein leads to the recruitment of Tead1 and Tcf3 [34], which in turn stimulates *Malat1* expression through binding of CpG island (Fig. 5e and f). Enhanced binding in this region in the PSF group was confirmed through ChIP assays targeting Tead1 and Tcf3 (Fig. 6d). Collectively, these results indicated that the PSF led to the demethylation of *Malat1* promoter and nuclear translocation of Yap1, together with Tead1 and Tcf3, promoted *Malat1* expression.

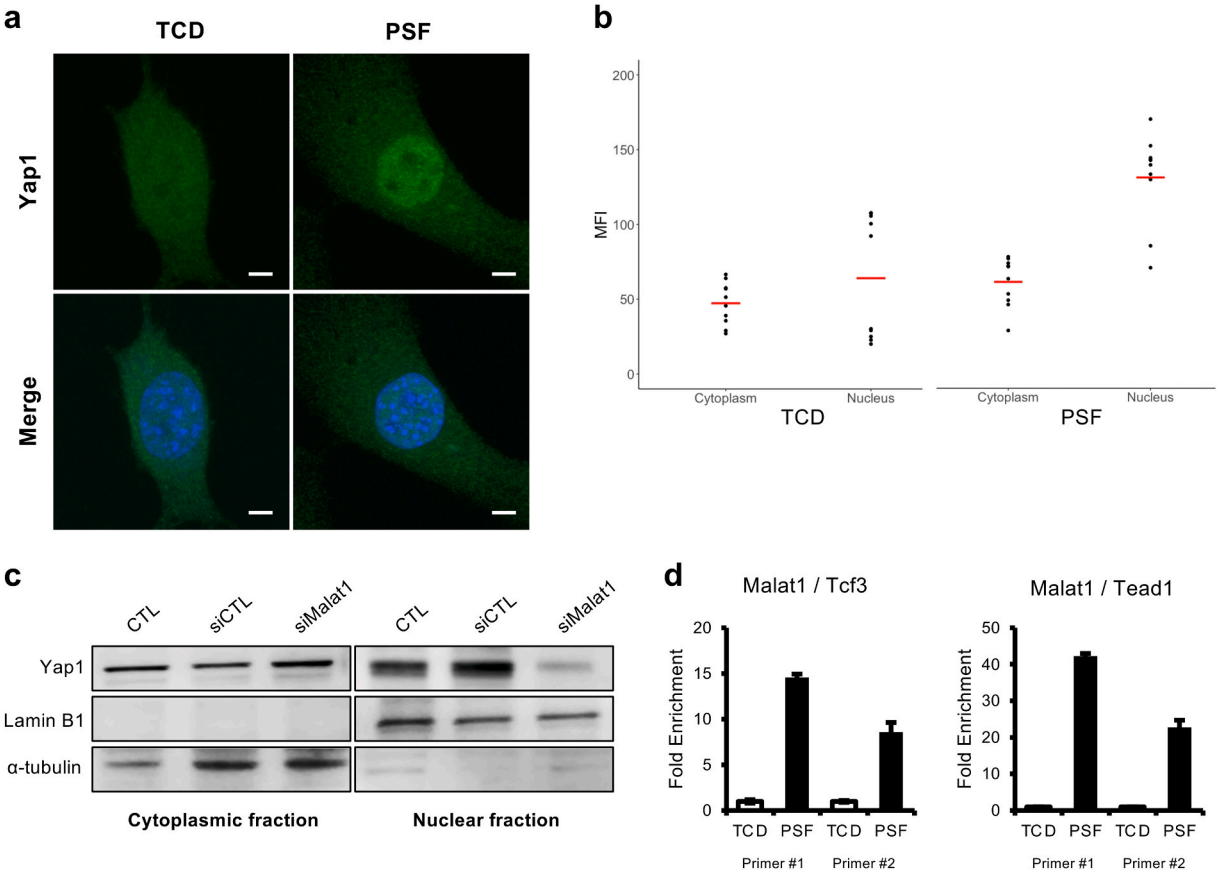

Fig. 6. PSF increases the nuclear translocation of Yap1 leading to *Malat1* expression.
(a) Immunofluorescence images described translocation of Yap1 protein into nucleus on PSF group. Scale bar = 10 μm (b) Quantitative analysis of immunofluorescence images of TCD and PSF respectively. (c, d) Chromatin immunoprecipitation (ChIP)-assay and ChIP-qPCR of Malat1/Tcf3 and Malat1/Tead1 binding. Fold enrichment was normalized using input. Translocation of Yap1 is observed in PSF and reverse effect is identified in siMalat1.

3.6. PSF-induced Malat1 elevates Piezo1 and enhances Yap1 nuclear translocation

In the PSF micro-environment, we noted an increased expression of the mechanosensitive Ca^{2+} ion channel *Piezo1* (Fig. 7a). This expression decreased following transfection with si*Malat1*, indicating that *Malat1* may regulate *Piezo1* for Ca^{2+} ion intake and concurrently up-regulate both *Piezo1* (Supplementary Fig. 6).

The nuclear translocation of Yap1 appears to occur via calcium-dependent signaling pathways. Live cell imaging was employed to monitor Ca^{2+} levels (orange, Rhod-2, AM) and showed much higher intracellular Ca^{2+} levels (orange, Rhod-2, AM) in the PSF group (Fig. 7b and c). It was notable that a calcineurin inhibitor cyclosporin A (CsA) decreased Yap1 translocation to nuclei (Fig. 7d and e), indicating that PSF-elicited high calcium levels facilitated Yap1 translocation.

3.7. Knockdown of Malat1 suppressed the PSF-induced osteogenic trans-differentiation

The knockdown of *Malat1* effectively diminished the influence of the Yap1-*Malat1* signal on the osteogenic trans-differentiation of myoblasts driven by PSF (Fig. 8a and Supplementary Fig. 7). The expressions of *Bmp2* and *Bmp7* were substantially decreased in the cells on PSF upon knockdown of *Malat1* (Fig. 8b). In turn, it was decreased the expression of bone marker genes such as *Runx2*, *Ocn*, and *Alp* (Fig. 8c).

Mechanistically, it was found that PSF induced a decrease in microRNAs (miRNAs) associated with osteogenic differentiation. In PSF, there was a reduction in the expression of several miRNAs. This includes miR-141, miR-100, miR-137, and miR-378a, all of which inhibit the expression of *Bmp2* and *Bmp7* [35–38]. Additionally, there was a decrease in the expression of miR-204 and miR-142a, which are related

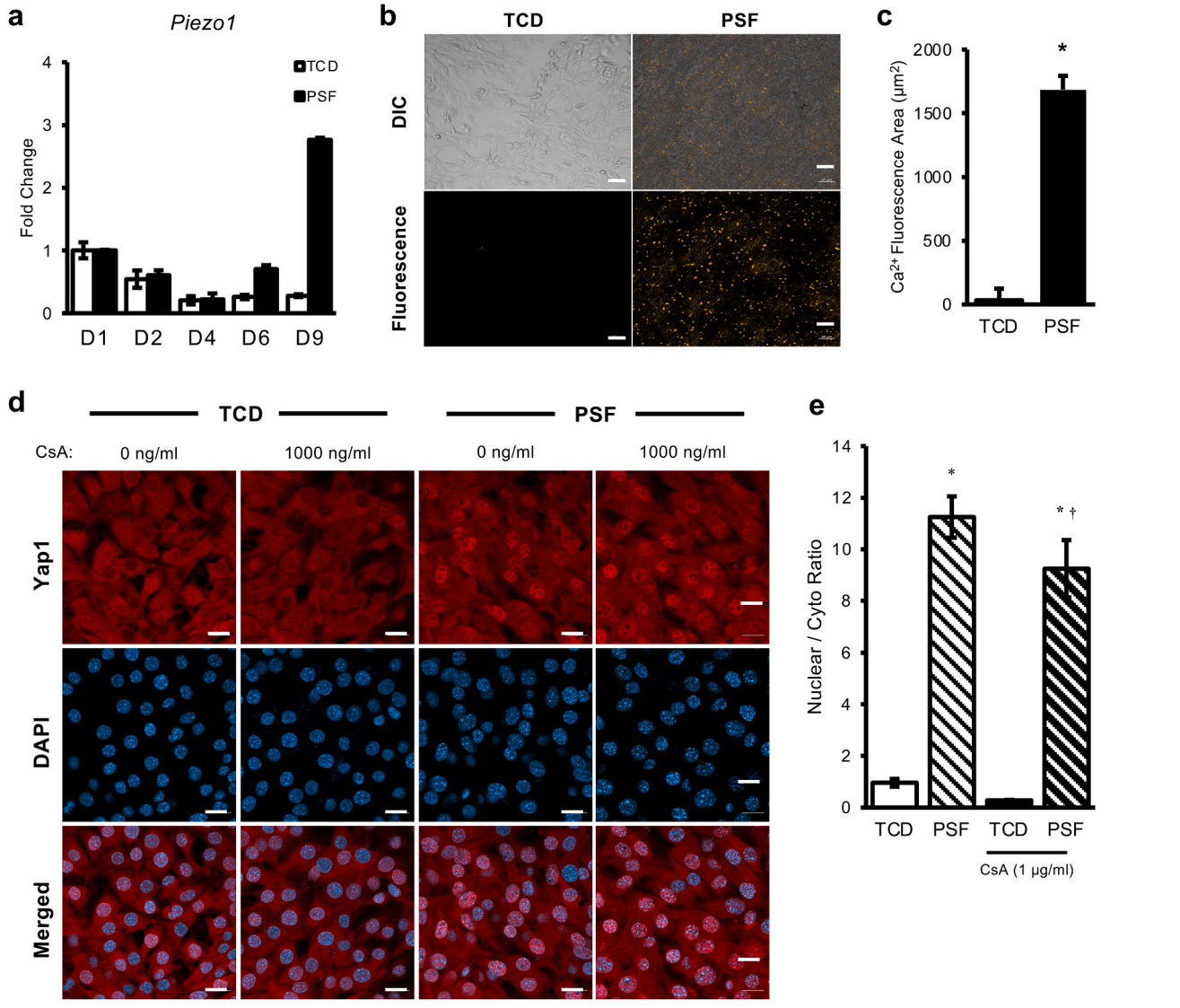

Fig. 7. *Malat1* elevates *Piezo1* expression and facilitates the nuclear translocation of Yap1 by increased intracellular Ca^{2+} levels.
(a) A time-course expression of *Piezo1* in C2C12 myoblasts cultures on PSF. (b) Live cell imaging of intracellular Ca^{2+} in the cells on PSF (orange, Rhod-2, AM) over 6 h. Scale bar = 500 μm. (c) Quantification of intracellular Ca^{2+}. Image analysis was performed by measuring the fluorescence area. (d-e) Immunofluorescence images of Yap1. The cells were treated with calcineurin inhibitor (cyclosporin A) at concentrations of 1000 ng/ml. Nuclear/Cyto ratio refers to the proportion of cells that have a Yap1-positive nucleus. Scale bar = 10 μm * Statistically different (TCD vs. PSF; $p < 0.05$). † Statistically different (Non-treated vs. CsA-treated; $p < 0.05$).

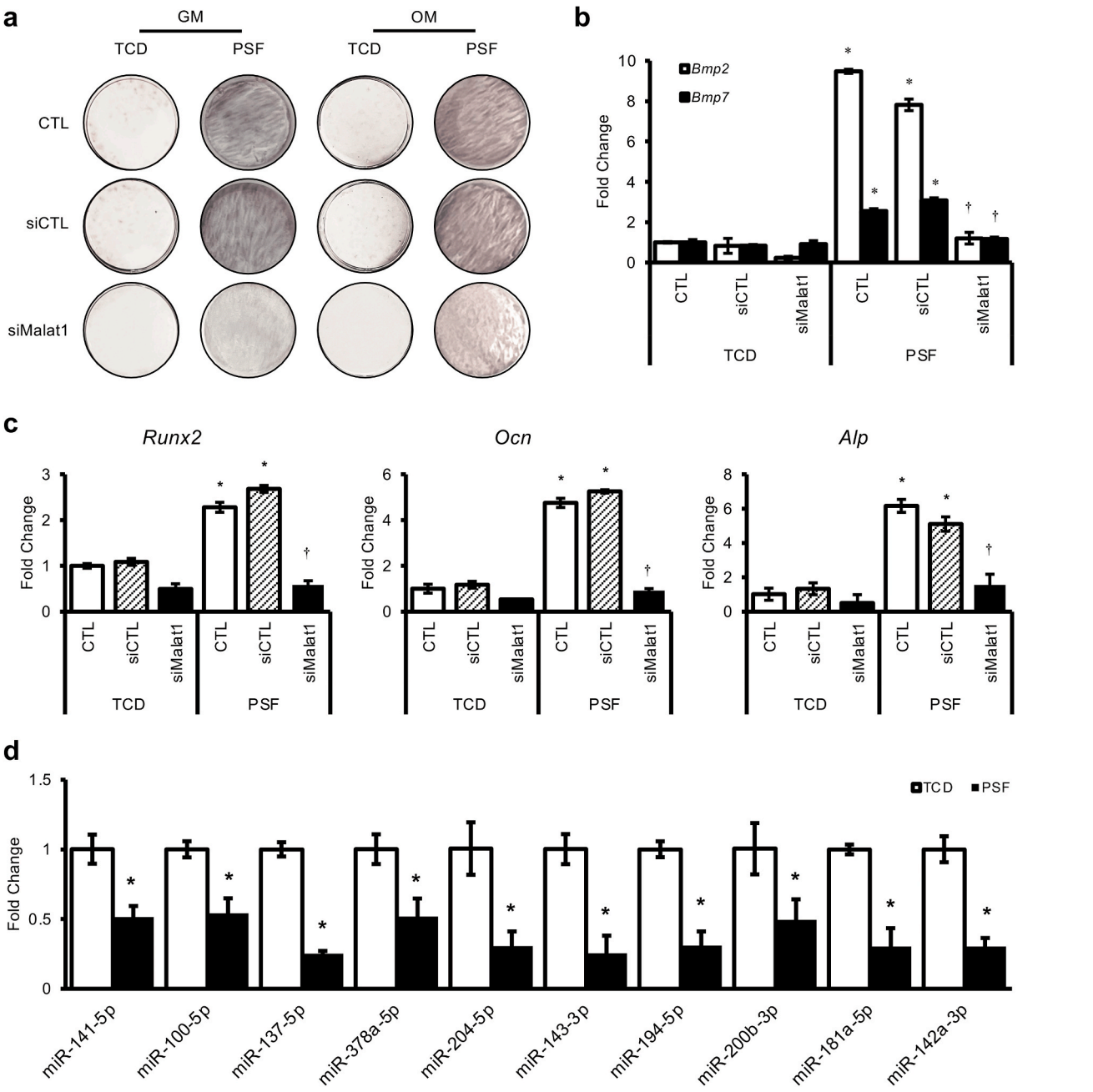

Fig. 8. Knockdown of *Malat1* attenuates PSF-induced osteogenic transdifferentiation of myoblasts through the regulation of microRNAs.
(a) ALP staining. The C2C12 cells were cultured for 4 days. (b) Expression of *Bmp2* and *Bmp7* transcripts determined by RT-qPCRs. (c) Expression of osteogenic marker genes determined by qPCRs. (d) Expression of miRNAs which *Malat1* regulate the level of. The miRNA RT-qPCR was performed in the cells cultured for 4 days (n = 3).

to SMAD signaling [39,40]. Similarly, the expression of miR-200b and miR-194, associated with YAP and Wnt signaling, was also diminished [41,42]. Furthermore, miR-143, known to inhibit the expression of *Osterix*, showed decreased levels [43]. In the other hand, miR-181a, which promotes myogenic differentiation, was also decreased [44] (Fig. 8d).

In summary, C2C12 myoblasts cultured on the ECM-mimicking PSF upregulated the expression of the long non-coding RNA *Malat1*, which was facilitated by mechanical stimuli-induced Yap1 signaling and the modulation of methylation levels at the CpG island in the promoter of *Malat1*. *Malat1* mediated osteogenic trans-differentiation through the regulation of miRNAs which transcriptionally control the expression of osteogenic/myogenic genes (Fig. 8d).

4. Discussion

This study aimed to elucidate the underlying causes of ectopic calcification induced by ECM mimicry in pathologic calcification. We investigated the ectopic calcification observed when PSF, known for its minimal bioreactivity, was implanted to an *in vivo* animal model. Similar osteogenic differentiation of C2C12, a myoblast precursor, was noted on the surface of PSF in *in vitro* experiments, and RNA-seq revealed the upregulation of the lncRNA *Malat1*. *Malat1* exhibited promoter demethylation as a result of epigenetic regulation under PSF conditions, with its expression being induced by the Yap1/Tead1/Tcf3 axis. Following this expression, *Malat1* prompted osteogenic differentiation via *Bmp2/7* signaling and induced the expression of *Piezo1*, which regulated Yap1

signaling through calcium channel signals in a positive feedback loop.

The PCs are chronic host-graft responses found in various medical contexts, such as heart valve transplants, vascular grafts, stent insertion, muscle transplants in volumetric muscle loss, and artificial joint transplants [45–48]. These reactions progress over the long term, often without an inflammatory response. Intriguingly, they can occur even without any inflammation or external stimuli from blood or immune cells, like cytokines or chemokines [49]. In such cases, ectopic calcification can develop as an active cell-mediated response to changes in the surface characteristics of biomaterials, not merely as a passive alteration, driven by epigenetic regulation mechanisms originating from the material surface. However, the specifics of these changes are not clearly understood. Also, intermuscular implantation serves as an appropriate *in vivo* model for evaluating the effects of the implant's 3D topography on muscle cells that are in direct contact with the implant. This model, however, has limitations in reflecting the hemodynamic, biological, and microbial factors observed in disease models such as heart valve or coronary artery graft models.

To replicate the fibrotic environment of PCs, we fabricated an electrospun PSF to mimic an ECM-like micro/nanofibrous architecture [50]. Polystyrene, being non-reactive by itself, is suitable for studying the physiological changes induced by fibrous topography [51]. In a manner akin to Zhang et al.'s ECM-like scaffold fabrication method, we generated a micro/nanofibrous architecture similar to the ECM by spinning polystyrene fibers, combining nano-to micro-scale sizes and arranging fiber orientations atypical for the material [25]. Additionally, various polymers and bioderived ECMs are utilized for fabricating ECM mimics. While bioderived ECMs such as Acellular Matrix offer structural superiority, they cannot completely eliminate the influence of biological factors. Polymer-based biomimetic materials, including PS used in this study, as well as polycaprolactone (PCL), polylactic-*co*-glycolic acid (PLGA), poly(propylene fumarate-*co*-ethylene glycol), poly(vinyl alcohol) (PVA), poly(acrylic acid) (PAA), and polyurethanes, employ various techniques such as 3D bioprinting, hydrogels, micropatterning, and electrospinning. Contrasting with the PSF, the smooth-surfaced PTFE, which has been used for long-term GBR procedures, did not induce PCs, thereby supporting the hypothesis that surface characteristics play a crucial role in the induction of PCs. To elucidate the model and mechanism, we conducted comparative experiments with a commercial control group lacking a 3D structure (*in vivo*: PTFE) (Fig. 2). We also tested if the same material with different surface properties shows spontaneous biological influences (*in vitro*: TCD) (Fig. 3). This highlights not only the substantial impact of implant surface structure on ectopic calcification but also explanation for the varied potential of long-term implanted materials to induce calcification.

YAP1 has emerged as a crucial mechano-regulated protein whose transcriptional activity is influenced by mechanical cues. Specifically, the YAP/TAZ signaling pathway has been linked to the ability of mesenchymal stem cells to transition to an osteogenic phenotype [52]. Associated with this mechano-transduction process, Piezo1 is a mechanosensitive ion channel protein that responds to mechanical stimuli. Recent research has demonstrated that Piezo1/2-mediated mechano--transduction is essential for bone formation through activation of the YAP1-associated pathway [53].

Long non-coding RNAs (lncRNAs), including Malat1, participate in diverse biological processes and have implications in various pathological conditions. Malat1, a highly conserved lncRNA, has been extensively studied in cancer, where it promotes cell proliferation, migration, and invasion, facilitating metastasis [54–56]. However, its influence extends beyond cancer and encompasses essential cellular functions. In the context of bone formation, it has been reported that Malat1 plays a significant role in enhancing osteoblast differentiation and mineralization [57]. Its overexpression correlates with increased bone mass and improved bone microarchitecture *in vivo* [58]. Malat1 achieves this by regulating key osteogenesis-promoting factors such as Runx2 and Bmp2 [59], acting as a molecular sponge for miRNAs that would otherwise inhibit these factors, thereby promoting bone formation [60]. Furthermore, Malat1 modulates the epigenetic profile of osteoblasts, interacting with the Polycomb Repressive Complex 2 (PRC2) responsible for histone protein methylation, a critical epigenetic modification affecting gene expression [61]. This suggests that *Malat1* orchestrates osteoblast differentiation at an epigenetic level, fine-tuning the expression of genes necessary for proper bone formation. Also, previous study reveals that *Malat1* regulates myogenic differentiation and muscle regeneration; suppressing it enhances muscle repair [44,62]. It also details a miR-181a-Malat1-MyoD/Suv39h1 regulatory axis involved in this process [44].

Previous research indicates that the Yap1 signaling pathway directly regulates Malat1, a long non-coding RNA involved in epithelial-mesenchymal transition (EMT) and bone differentiation. *Yap1* enhances *Malat1* expression by binding to its promoter with the Tcf4/β-catenin complex, while the Yap-SRSF1 complex suppresses it [63]. In bone formation, *Malat1* acts as a miRNA sponge and epigenetic regulator, promoting osteogenic differentiation [64]. However, the specific mechanisms by which Yap1 and Malat1 induce osteogenic differentiation remain unknown, suggesting an area for further exploration.

There is currently no standardized target for treating PCs, although various potential treatments have been explored based on basic biology, physical chemistry, or empirical patient observations [10]. Based on the calcification induced by implanted PSF in this study, *Malat1* emerged as a crucial target for pathologic ectopic calcification, where it modulated the Yap1/Tead1/Tcf3 signaling axis. Our results shed light on potential novel mechanisms and treatments for pathological calcification caused by fibrotic surface structures of prostheses.

5. Conclusion

In conclusion, our study reveals that the transplantation of heterogenous polystyrene nanofibers (PSF) induces ectopic calcification *in vivo*, demonstrating the impact of its ECM-mimicking 3D topology. Additionally, PSF influences myoblasts to undergo osteogenic differentiation without external signals. The upregulation of long non-coding RNA *Malat1* on PSF plays a pivotal role in orchestrating osteogenic *trans*-differentiation through demethylation of its promoter, Yap1 signaling activation, and regulation of key miRNAs. These findings provide insights into the molecular mechanisms governing PSF's influence on cellular behavior, with potential implications for tissue engineering and regenerative medicine.

CRediT authorship contribution statement

Woo-Jin Kim: Writing – review & editing, Writing – original draft, Formal analysis, Data curation, Conceptualization. **Jieun Bae:** Visualization, Validation, Methodology, Investigation, Formal analysis. **Eun-Hye Lee:** Investigation, Formal analysis. **Jaehyung Kim:** Investigation. **Pil-Jong Kim:** Formal analysis, Data curation. **Peter X. Ma:** Writing – review & editing, Data curation. **Kyung Mi Woo:** Writing – review & editing, Supervision, Project administration, Conceptualization.

Declaration of competing interest

The authors declare that they have no known competing financial interests or personal relationships that could have appeared to influence the work reported in this paper.

Data availability

Data will be made available on request.

Acknowledgement

The late Dr. Joung-Hwan Oh dedicated to this work. The authors

wish to acknowledge the financial support from National Research Foundation of Korea (NRF-2018R1A5A2024418, NRF-2019R1A2C2008113).

Appendix A. Supplementary data

Supplementary data to this article can be found online at https://doi.org/10.1016/j.mtbio.2024.101182.

References

[1] M.D. Francis, R.G. Russell, H. Fleisch, Diphosphonates inhibit formation of calcium phosphate crystals in vitro and pathological calcification in vivo, Science 165 (1969) 1264–1266, https://doi.org/10.1126/science.165.3899.1264.

[2] H.C. Anderson, Mechanisms of pathologic calcification, Rheum Dis Clin North Am 14 (1988) 303–319.

[3] A. Kostyunin, et al., Ultrastructural pathology of atherosclerosis, calcific aortic valve disease, and bioprosthetic heart valve degeneration: commonalities and differences, Int. J. Mol. Sci. 21 (2020), https://doi.org/10.3390/ijms21207434.

[4] S. Wen, et al., Mechanisms and drug therapies of bioprosthetic heart valve calcification, Front. Pharmacol. 13 (2022) 909801, https://doi.org/10.3389/fphar.2022.909801.

[5] Hervé Kempf, Svetlana Komarova, Monzur Murshed, Editorial: ectopic mineralization of tissues: mechanisms, risk factors, diseases, and prevention, Front. Cell Dev. Biol. 25 (9) (2021 Oct) 759702, https://doi.org/10.3389/fcell.2021.759702.eCollection.2021.

[6] K. Hoshi, S. Kemmotsu, Y. Takeuchi, N. Amizuka, H. Ozawa, The primary calcification in bones follows removal of decorin and fusion of collagen fibrils, J. Bone Miner. Res. 14 (2) (1999) 273–280, https://doi.org/10.1359/jbmr.1999.14.2.273.

[7] A. Huang, G. Guo, Y. Yu, L. Yao, The roles of collagen in chronic kidney disease and vascular calcification, Journal of Molecular Medicine 99 (1) (2020) 75–92, https://doi.org/10.1007/s00109-020-02014-6.

[8] E. Jover, A. Silvente, F. Marin, J. Martinez-Gonzalez, M. Orriols, C.M. Martinez, C. M. Puche, M. Valdés, C. Rodriguez, D. Hernández-Romero, Inhibition of enzymes involved in collagen cross-linking reduces vascular smooth muscle cell calcification, Faseb. J. 32 (8) (2018) 4459–4469, https://doi.org/10.1096/fj.201700653r.

[9] L. Yu, M. Wei, Biomineralization of collagen-based materials for hard tissue repair, Int. J. Mol. Sci. 22 (2) (2021) 944, https://doi.org/10.3390/ijms22020944.

[10] N. Vidavsky, J. Kunitake, L.A. Estroff, Multiple pathways for pathological calcification in the human body, Adv Healthc Mater 10 (2021) e2001271, https://doi.org/10.1002/adhm.202001271.

[11] C.Y. Yip, C.A. Simmons, The aortic valve microenvironment and its role in calcific aortic valve disease, Cardiovasc. Pathol. 20 (2011) 177–182, https://doi.org/10.1016/j.carpath.2010.12.001.

[12] A. Denchai, D. Tartarini, E. Mele, Cellular response to surface morphology: electrospinning and computational modeling, Front. Bioeng. Biotechnol. 6 (2018) 155, https://doi.org/10.3389/fbioe.2018.00155.

[13] S.U. Rahman, et al., Fibrous topography-potentiated canonical Wnt signaling directs the odontoblastic differentiation of dental pulp-derived stem cells, ACS Appl. Mater. Interfaces 10 (2018) 17526–17541, https://doi.org/10.1021/acsami.7b19782.

[14] J. Song, et al., Controlled surface topography regulates collective 3D migration by epithelial-mesenchymal composite embryonic tissues, Biomaterials 58 (2015) 1–9, https://doi.org/10.1016/j.biomaterials.2015.04.021.

[15] A. Prasopthum, M. Cooper, K.M. Shakesheff, J. Yang, Three-dimensional printed scaffolds with controlled micro-/nanoporous surface topography direct chondrogenic and osteogenic differentiation of mesenchymal stem cells, ACS Appl. Mater. Interfaces 11 (2019) 18896–18906, https://doi.org/10.1021/acsami.9b01472.

[16] J. Chanda, K. Kondoh, K. Ijima, M. Matsukawa, R. Kuribayashi, In vitro and in vivo calcification of vascular bioprostheses, Biomaterials 19 (1998) 1651–1656, https://doi.org/10.1016/s0142-9612(98)00038-6.

[17] J.A. Brown, et al., Structural insights into the stabilization of MALAT1 noncoding RNA by a bipartite triple helix, Nat. Struct. Mol. Biol. 21 (2014) 633–640, https://doi.org/10.1038/nsmb.2844.

[18] J. Kim, et al., Long noncoding RNA MALAT1 suppresses breast cancer metastasis, Nat. Genet. 50 (2018) 1705–1715, https://doi.org/10.1038/s41588-018-0252-3.

[19] R. Ebrahimi, et al., Adipose tissue gene expression of long non-coding RNAs; MALAT1, TUG1 in obesity: is it associated with metabolic profile and lipid homeostasis-related genes expression? Diabetol Metab Syndr 12 (2020) 36, https://doi.org/10.1186/s13098-020-00544-0.

[20] N. Was, M. Sauer, U. Fischer, M. Becker, lncRNA Malat1 and miR-26 cooperate in the regulation of neuronal progenitor cell proliferation and differentiation, RNA 29 (2022) 69–81, https://doi.org/10.1261/rna.079436.122.

[21] Y. Zhang, et al., METTL3 mediated MALAT1 m6A modification promotes proliferation and metastasis in osteosarcoma cells, Mol. Biotechnol. (2023), https://doi.org/10.1007/s12033-023-00953-2.

[22] Y.Z. Chang, et al., METTL3 enhances the stability of MALAT1 with the assistance of HuR via m6A modification and activates NF-kappaB to promote the malignant progression of IDH-wildtype glioma, Cancer Lett. 511 (2021) 36–46, https://doi.org/10.1016/j.canlet.2021.04.020.

[23] J. Han, et al., Bioresponsive immunotherapeutic materials, Adv Mater (2023) e2209778, https://doi.org/10.1002/adma.202209778.

[24] J.O. You, D. Almeda, G.J. Ye, D.T. Auguste, Bioresponsive matrices in drug delivery, J. Biol. Eng. 4 (2010) 15, https://doi.org/10.1186/1754-1611-4-15.

[25] Q. Zhang, et al., Effects of the fibrous topography-mediated macrophage phenotype transition on the recruitment of mesenchymal stem cells: an in vivo study, Biomaterials 149 (2017) 77–87, https://doi.org/10.1016/j.biomaterials.2017.10.007.

[26] F. Krueger, S.R. Andrews, Bismark: a flexible aligner and methylation caller for Bisulfite-Seq applications, Bioinformatics 27 (2011) 1571–1572, https://doi.org/10.1093/bioinformatics/btr167.

[27] B.I. Laufer, et al., Low-pass whole genome bisulfite sequencing of neonatal dried blood spots identifies a role for RUNX1 in Down syndrome DNA methylation profiles, Hum. Mol. Genet. 29 (2021) 3465–3476, https://doi.org/10.1093/hmg/ddaa218.

[28] X. Zhu, W. Cui, X. Li, Y. Jin, Electrospun fibrous mats with high porosity as potential scaffolds for skin tissue engineering, Biomacromolecules 9 (2008) 1795–1801, https://doi.org/10.1021/bm800476u.

[29] M. Abudhahir, et al., Polycaprolactone fibrous electrospun scaffolds reinforced with copper doped wollastonite for bone tissue engineering applications, J. Biomed. Mater. Res. B Appl. Biomater. 109 (2021) 654–664, https://doi.org/10.1002/jbm.b.34729.

[30] G. Thinakaran, J. Ojala, J. Bag, Expression of c-jun/AP-1 during myogenic differentiation in mouse C2C12 myoblasts, FEBS Lett. 319 (1993) 271–276, https://doi.org/10.1016/0014-5793(93)80561-8.

[31] M. Kawai, K. Bessho, H. Maruyama, J. Miyazaki, T. Yamamoto, Simultaneous gene transfer of bone morphogenetic protein (BMP) -2 and BMP-7 by in vivo electroporation induces rapid bone formation and BMP-4 expression, BMC Musculoskelet Disord 7 (2006) 62, https://doi.org/10.1186/1471-2474-7-62.

[32] N. Yamamoto, et al., Smad1 and smad5 act downstream of intracellular signalings of BMP-2 that inhibits myogenic differentiation and induces osteoblast differentiation in C2C12 myoblasts, Biochem. Biophys. Res. Commun. 238 (1997) 574–580, https://doi.org/10.1006/bbrc.1997.7325.

[33] L. Shum, X. Wang, A.A. Kane, G.H. Nuckolls, BMP4 promotes chondrocyte proliferation and hypertrophy in the endochondral cranial base, Int. J. Dev. Biol. 47 (2003) 423–431.

[34] J.H. Koo, K.L. Guan, Interplay between YAP/TAZ and metabolism, Cell Metab 28 (2018) 196–206, https://doi.org/10.1016/j.cmet.2018.07.010.

[35] B. Yanagawa, et al., miRNA-141 is a novel regulator of BMP-2-mediated calcification in aortic stenosis, J. Thorac. Cardiovasc. Surg. 144 (2012) 256–262, https://doi.org/10.1016/j.jtcvs.2011.10.097.

[36] R. Wang, et al., MiR-100-5p inhibits osteogenic differentiation of human bone mesenchymal stromal cells by targeting TMEM135, Hum. Cell 35 (2022) 1671–1683, https://doi.org/10.1007/s13577-022-00764-8.

[37] X. Ying, Y. Sun, P. He, MicroRNA-137 inhibits BMP7 to enhance the epithelial-mesenchymal transition of breast cancer cells, Oncotarget 8 (2017) 18348–18358, https://doi.org/10.18632/oncotarget.15442.

[38] Y. Tang, T.A. Shah, E.J. Yurkow, M.B. Rogers, MicroRNA profiles in calcified and healthy aorta differ: therapeutic impact of miR-145 and miR-378, Physiol Genomics (2020), https://doi.org/10.1152/physiolgenomics.00074.2020.

[39] X. Xiao, et al., LncRNA MALAT1 sponges miR-204 to promote osteoblast differentiation of human aortic valve interstitial cells through up-regulating Smad4, Int. J. Cardiol. 243 (2017) 404–412, https://doi.org/10.1016/j.ijcard.2017.05.037.

[40] Q. Yu, et al., MALAT1 functions as a competing endogenous RNA to regulate SMAD5 expression by acting as a sponge for miR-142-3p in hepatocellular carcinoma, Cell Biosci. 9 (2019) 39, https://doi.org/10.1186/s13578-019-0299-6.

[41] N. Han, W. Tian, N. Yu, L. Yu, YAP1 is required for the angiogenesis in retinal microvascular endothelial cells via the inhibition of MALAT1-mediated miR-200b-3p in high glucose-induced diabetic retinopathy, J. Cell. Physiol. 235 (2020) 1309–1320, https://doi.org/10.1002/jcp.29047.

[42] L. Gu, J. Liu, D. Xu, Y. Lu, Reciprocal feedback loop of the MALAT1-MicroRNA-194-YAP1 pathway regulates progression of acute pancreatitis, Med Sci Monit 25 (2019) 6894–6904, https://doi.org/10.12659/MSM.915598.

[43] R. Wang, et al., miR-143 promotes angiogenesis and osteoblast differentiation by targeting HDAC7, Cell Death Dis. 11 (2020) 179, https://doi.org/10.1038/s41419-020-2377-4.

[44] X. Chen, et al., Malat1 regulates myogenic differentiation and muscle regeneration through modulating MyoD transcriptional activity, Cell Discov 3 (2017) 17002, https://doi.org/10.1038/celldisc.2017.2.

[45] M.E. Guerrero, et al., Diagnosis, classification, and management strategies for mitral annular calcification: a heart valve collaboratory position statement, JACC Cardiovasc. Interv. 16 (2023) 2195–2210, https://doi.org/10.1016/j.jcin.2023.06.044.

[46] A. Lejay, et al., Calcification of synthetic vascular grafts: a systematic review, EJVES Vasc Forum 60 (2023) 1–7, https://doi.org/10.1016/j.ejvsvf.2023.05.013.

[47] M.J.H. van Oort, et al., Procedural and clinical impact of intravascular lithotripsy for the treatment of peri-stent calcification, Cardiovasc Revasc Med (2023), https://doi.org/10.1016/j.carrev.2023.10.013.

[48] N.A. Mignemi, et al., Plasmin prevents dystrophic calcification after muscle injury, J. Bone Miner. Res. 32 (2017) 294–308, https://doi.org/10.1002/jbmr.2973.

[49] S. Xu, et al., Mechanism analysis of vascular calcification based on fluid dynamics, Diagnostics 13 (2023), https://doi.org/10.3390/diagnostics13162632.

[50] M. Keshvardoostchokami, et al., Electrospun nanofibers of natural and synthetic polymers as artificial extracellular matrix for tissue engineering, Nanomaterials 11 (2020), https://doi.org/10.3390/nano11010021.

[51] M. El Fray, P. Prowans, J.E. Puskas, V. Altstadt, Biocompatibility and fatigue properties of polystyrene-polyisobutylene-polystyrene, an emerging thermoplastic elastomeric biomaterial, Biomacromolecules 7 (2006) 844–850, https://doi.org/10.1021/bm050971c.
[52] S. Dupont, et al., Role of YAP/TAZ in mechanotransduction, Nature 474 (2011) 179–183, https://doi.org/10.1038/nature10137.
[53] T. Zhou, et al., Piezo1/2 mediate mechanotransduction essential for bone formation through concerted activation of NFAT-YAP1-ss-catenin, Elife 9 (2020), https://doi.org/10.7554/eLife.52779.
[54] Z. Liao, et al., LncRNA MALAT1-targeting antisense oligonucleotide ameliorates the AngII-induced vascular smooth muscle cell proliferation and migration via Nrf2/GPX4 antioxidant pathway, J. Cardiovasc. Pharmacol. (2023), https://doi.org/10.1097/FJC.0000000000001521.
[55] J. Wang, G. Yao, B. Zhang, Z. Zhao, Y. Fan, Interaction between miR-206 and lncRNA MALAT1 in regulating viability and invasion in hepatocellular carcinoma, Oncol. Lett. 27 (2024) 5, https://doi.org/10.3892/ol.2023.14138.
[56] X. Wang, et al., N(6)-methyladenosine modification of MALAT1 promotes metastasis via reshaping nuclear speckles, Dev. Cell 56 (2021) 702–715 e708, https://doi.org/10.1016/j.devcel.2021.01.015.
[57] Y. Gao, et al., Long noncoding RNA MALAT1 promotes osterix expression to regulate osteogenic differentiation by targeting miRNA-143 in human bone marrow-derived mesenchymal stem cells, J. Cell. Biochem. 119 (2018) 6986–6996, https://doi.org/10.1002/jcb.26907.
[58] J. Yin, et al., lncRNA MALAT1 mediates osteogenic differentiation of bone mesenchymal stem cells by sponging miR-129-5p, PeerJ 10 (2022) e13355, https://doi.org/10.7717/peerj.13355.
[59] J. Li, et al., lncRNAs MALAT1 and LINC00657 upstream to miR-214-3p/BMP2 regulate osteogenic differentiation of human mesenchymal stem cells, Mol. Biol. Rep. 49 (2022) 6847–6857, https://doi.org/10.1007/s11033-022-07136-3.
[60] Y. Zhou, Z. Xu, Y. Wang, Q. Song, R. Yin, LncRNA MALAT1 mediates osteogenic differentiation in osteoporosis by regulating the miR-485-5p/WNT7B axis, Front. Endocrinol. 13 (2022) 922560, https://doi.org/10.3389/fendo.2022.922560.
[61] J. Yi, D. Liu, J. Xiao, LncRNA MALAT1 sponges miR-30 to promote osteoblast differentiation of adipose-derived mesenchymal stem cells by promotion of Runx2 expression, Cell Tissue Res. 376 (2019) 113–121, https://doi.org/10.1007/s00441-018-2963-2.
[62] D. Li, et al., Long non-coding RNA MALAT1 promotes cardiac remodeling in hypertensive rats by inhibiting the transcription of MyoD, Aging (Albany NY) 11 (2019) 8792–8809, https://doi.org/10.18632/aging.102265.
[63] J. Matuszyk, MALAT1-miRNAs network regulate thymidylate synthase and affect 5FU-based chemotherapy, Mol Med 28 (2022) 89, https://doi.org/10.1186/s10020-022-00516-2.
[64] X. Huang, S. Jie, W. Li, C. Liu, GATA4-activated lncRNA MALAT1 promotes osteogenic differentiation through inhibiting NEDD4-mediated RUNX1 degradation, Cell Death Discov 9 (2023) 150, https://doi.org/10.1038/s41420-023-01422-0.